

# Ultrafast Laser Pulse Control of Exciton Dynamics: A Computational Study on the FMO Complex<sup>†</sup>

Ben Brüggemann and Volkhard May\*

*Institut für Physik, Humboldt Universität zu Berlin, Newtonstrasse 15, D-12489 Berlin, Germany*

*Received: February 4, 2004; In Final Form: May 23, 2004*

Femtosecond laser-pulse-induced spatial localization of excitation energy in the FMO complex is suggested theoretically. Based on the Frenkel exciton model for the bacteriochlorophyll (BChl)  $Q_y$ -excitations, the laser-pulse-driven exciton wave packet motion into a single, spatially localized  $Q_y$  state is described in detail. First, the manner in which excitation energy relaxation and dephasing, as well as the length and overall intensity of the control pulse, determine the control yield is discussed. In a next step, two-exciton states decaying via exciton–exciton annihilation are included, and a preliminary attempt is undertaken to account for structural and energetic disorder. Although the latter effects may decrease the efficiency of excitation energy localization drastically, it is demonstrated that, even under realistic conditions, tailored laser pulses may deposit energy in a single BChl of the FMO complex.

## I. Introduction

It is of ongoing interest to study femtosecond laser pulse control of molecular dynamics. Because an experimental realization could be demonstrated for a variety of systems, the entire field moved away from a pure theoretical speculation to a feasible experimental approach (for a recent overview, see refs 1–4). Laser pulse control has been suggested in the theoretical works of Tannor, Kosloff, and Rice<sup>5</sup> and Brumer and Shapiro.<sup>6</sup> The theory was put into the universal frame of the so-called Optimal Control Theory (OCT) by Rabitz.<sup>7,8</sup> However, until the use of complex pulse shaping systems, the approaches to achieve an experimental demonstration were less successful. Currently, the combination of a liquid-crystal or opto-acoustic femtosecond pulse shaper with a feedback control of the outcome represents a powerful tool for addressing various control tasks.<sup>4</sup> Although originally concentrated on gas-phase systems, examples have been also reported for the pulse control of polyatomic molecules, as well as molecules in the condensed phase<sup>9,10</sup> and even biological systems.<sup>11</sup>

In the standard scheme of laser pulse control, one tries to form a certain vibrational wave packet, which should move into a predefined target state. Typically, this might be a nonbonding electronic state that corresponds to the removal of a certain part of the molecule. In the present paper, however, we will discuss a somewhat different type of control task: the formation of an electronic (excitonic) wave packet in a chromophore complex and the laser-pulse-guided spatial localization of the respective excitation energy within one chromophore. Some preliminary discussions of this suggestion have been already given in the work of Mancal and co-workers.<sup>12,13</sup>

The basic idea discussed here is similar to the attempt to localize vibrational excitation energy in a particular bond (cf, e.g., refs 1 and 2). Such a local vibrational excitation does not represent an eigenstate of the respective molecular system but is given as a certain superposition of eigenstates. Through

application of an external laser pulse, it becomes possible to prepare such a superposition state (wave packet). The short duration of the pulse (often definitely <100 fs) and the related spectral broadening allows one to excite a coherent superposition of states and move the related wave packet in the target state at the required time. In the present paper, we will answer the question whether excitation energy localization is reliable when translated to electronic (excitonic) wave packets.

To realize such a control task, one requires systems where the interchromophore coupling overcomes vibrational relaxation, at least within a certain time interval. Just for such systems, we can expect wave packet formation and its coherent driving by the externally applied field. Furthermore, optical addressability of any exciton level is the precondition for the formation of a flexible wave packet. This requires systems with a well-balanced distribution of the entire oscillator strength across all exciton levels. If it is only possible to exclusively excite a single-exciton level (because of symmetry reasons), the entire concept will fail. We also refer to the unfavorable influence of disorder. Probably, the compromise that the control laser must make among molecules with different spatial and energetic structure would become too large to solve the control task.

There are different chromophore complex candidates that fulfill this demand. Because of its well-defined structure, we choose a biological example: the FMO complex (cf. Figure 1). It represents a pigment protein complex of the green sulfur bacteria photosynthetic apparatus (cf., e.g., van Amerongen et al.<sup>15</sup> and the recent measurements of the Small group<sup>16,17</sup>). The FMO complex in its trimeric form covers 21 bacteriochlorophyll-a (BChl) molecules; thus, a monomer with 7 BChl is of a modest extent and is well-suited for the present discussion. Incidentally, the need for a distribution of oscillator strength across all exciton levels favors the FMO complex with its spatially distributed BChl against high-symmetric arrangements of chromophores, as in the light-harvesting complexes of purple bacteria (LH1 and LH2) or in linear dye aggregates.

Of course, when considering chromophore complexes under the action of an intensive optical field, higher exciton states (multiexciton states) must be taken into consideration (or at least

<sup>†</sup> Part of the special issue “Gerald Small Festschrift”.

\* Author to whom correspondence should be addressed. E-mail address: may@physik.hu-berlin.de.

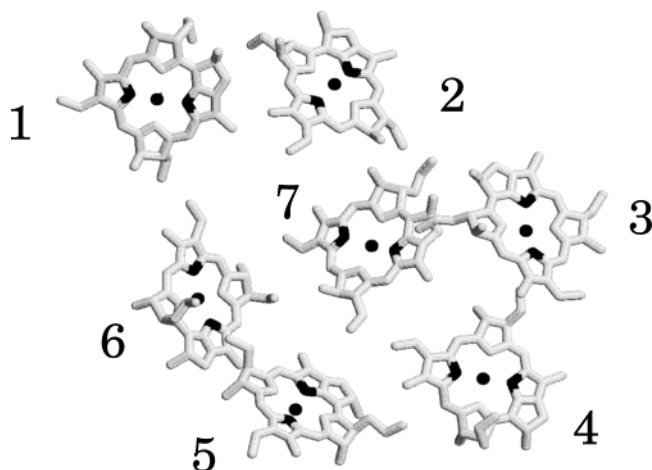


**Figure 1.** Depiction of the arrangement of the seven BChls in the FMO complex, using the structural data from ref 18 (identifier 4BCL in the Protein Data Bank, rotated for better view). Atoms in the line of the respective  $Q_y$ -dipole moments are marked (plotted with rasmol).

the possibility to populate the two-exciton manifold must be considered). Now, the formation of a (single-)exciton wave packet and the subsequent trial of spatial localization are accompanied by optical transitions into two-exciton states. One expects the formation of a single-exciton wave packet, as well as a two-exciton wave packet, but possibly it all moves (via stimulated recombination from the two-exciton state to the single-exciton state) into a single excited chromophore state. We also will account for this mechanism in achieving control in the following. As it is known from different studies on laser pulse control, excitation energy relaxation and dephasing represent an additional obstacle. (See, for example, ref 13.) In the present case, dissipation enters via exciton-vibrational coupling. If it is not too strong, it can be described via a density matrix that has been reduced to the electronic (excitonic) degrees of freedom of the system. Such an approach has been developed in, e.g., refs 19–21 (together with exciton exciton annihilation) and will be used here.

Before giving an overview on the applied density matrix theory, we start with a brief foundation of the multiexciton (MX) model for the FMO complex (details can be found in Appendix A). Section III then explains how to compute the laser pulse that achieves spatial excitation energy localization. The results of our simulations are discussed in Section IV, and some conclusions are drawn in Section V.

## II. Multiexciton Dynamics in the FMO Complex

To study laser-pulse-driven excitation energy dynamics in the FMO complex, it is most appropriate to describe the electronic excited-state levels according to the MX scheme.<sup>19–21</sup> Within such an approach, a common description of the Coulombic interchromophore coupling, and of the various dissipation channels, is achieved. The feasibility of this MX theory has been demonstrated at different places (see, e.g., refs 22 and 23). The MX scheme starts with the electronic ground state of the complex  $|0\rangle$  and is followed by the (single) exciton states  $|\alpha_1\rangle$ . In the present case, they correspond to a single, but probably delocalized,  $Q_y$ -excitation. If a single exciton state has been excited via single-photon absorption, the absorption of an additional photon may lead to the formation of one of the two-exciton states  $|\beta_2\rangle$ . These states result from the presence of two  $Q_y$ -excitations at different BChl or of a higher excitation at a

single BChl. The two-exciton states are followed by three-exciton states  $|\gamma_3\rangle$  and so on. MX energy relaxation and dephasing is induced by a coupling to intra-BChl as well as protein vibrations. The overall laser-pulse-driven dissipative MX dynamics will be taken into consideration in a description known as the quantum master equation or the multilevel Redfield theory and is based on the (reduced) MX density matrix.

This all has been explained in detail in ref 19 and is shortly reviewed in Appendix A. The specification to the monomeric FMO complex is straightforward. Here, we will follow mainly refs 19 and 22, as well as our own recent extensions<sup>20,24</sup> on the inclusion of exciton–exciton annihilation (EEA). Although less is known on the importance of EEA in the FMO complex, in any case, it represents an important de-excitation channel when considering two-exciton states and should be taken into consideration.

### II.A. Single- and Two-Exciton States of the FMO Complex

In specifying the MX approach to the FMO complex, we introduce a three-level model for each of the seven BChl (a schematic view of the FMO complex is given in Figure 1, along with the numbering scheme used to count the seven BChl). The model includes the ground state ( $\varphi_g$ ), the  $Q_y$  excited state (denoted as  $\varphi_e$ ), and a higher excited state ( $\varphi_f$ ). The  $\varphi_f$  state must be considered to be a representative of the multitude of higher excited electron-vibrational BChl states. Its introduction is motivated by the need to have BChl levels that are almost degenerated with the energy of a simultaneous presence of two  $Q_y$ -excitations at different BChl and allow for intra-BChl excited-state absorption. Consequently,  $\varphi_f$  is defined by the demand to be energetically similar positioned above  $\varphi_e$ , as  $\varphi_e$  is positioned above the ground state. The respective energies are denoted as  $\epsilon_{ma}$ , with  $m$  labeling the spatial position (site) in the FMO complex (cf. Figure 1), and we introduced  $a = g, e, f$ . These site energies differ one from another because of the different protein environment. However, in any case, we set  $\epsilon_{mf} - \epsilon_{me} = \epsilon_{me} - \epsilon_{mg}$ .

Besides their energy-level structure, every BChl must be characterized by transition-dipole moments. We assume that the magnitude of the  $Q_y$ -transition dipole moments ( $\mathbf{d}_m(eg)$ ) should be the same for all BChl, i.e., we have  $|\mathbf{d}_m(eg)| = |\mathbf{d}_n(eg)| = 6.4$  D. Of course, their spatial orientations differ. For the transition into the higher-excited BChl state, we set  $\mathbf{d}_m(fe) = \mathbf{d}_m(eg)$  for all  $m$ , i.e., for every BChl, the magnitude as well as the spatial orientation of the transition-dipole moments into the higher state is identical with those into the  $Q_y$ -state (cf. ref 22). Such a choice is mainly motivated by the fact that the states  $\varphi_f$  represent a multitude of higher excited BChl electron-vibrational states. Moreover, this assumption implies that the dipole–dipole interaction matrix  $J$ , which couples the transitions between the levels  $\epsilon_{mg}$  and  $\epsilon_{me}$  at BChl  $m$  with the transitions between the levels  $\epsilon_{ne}$  and  $\epsilon_{ng}$  at BChl  $n$  is identical with that leading at site  $n$  to the transition from  $\epsilon_{ne}$  to  $\epsilon_{nf}$ .

Having these data available, one can compute MX energies and states. Because all the following considerations are only concentrated on the single-exciton and two-exciton manifolds of the monomeric FMO complex, we will denote the single exciton quantum numbers  $\alpha_1$  by  $\alpha$ , and the  $\alpha_2$  numbers for two-exciton states by  $\tilde{\alpha}$ . The single exciton states are simply obtained as

$$|\alpha\rangle = \sum_m C_\alpha(m) |m e\rangle \quad (1)$$

where  $|m e\rangle$  describes the state of the FMO complex with a single  $Q_y$ -excitation at BChl  $m$ .  $\alpha$  runs from 1 to  $N_{\text{BChl}} = 7$

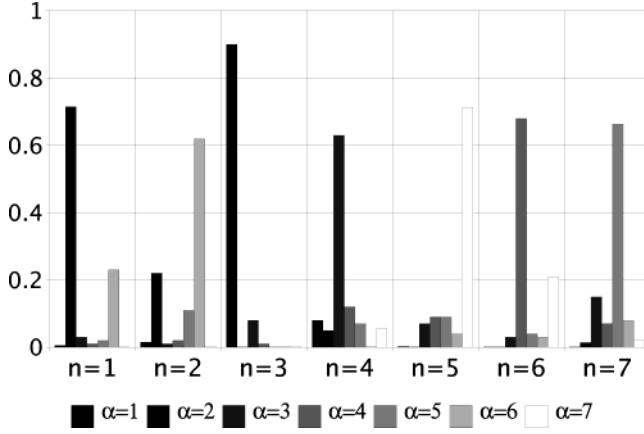


**Figure 2.** Exciton expansion coefficients  $|C_\alpha(n)|^2$  of the used FMO exciton model.

**TABLE 1: Energies of the BChls<sup>a</sup>**

$n$	energy, $\epsilon_n$	
	(cm <sup>-1</sup> )	(nm)
1	12 350	809.7
2	12 465	802.2
3	12 160	822.4
4	12 350	809.7
5	12 600	793.7
6	12 480	801.3
7	12 460	802.6

<sup>a</sup> See ref 23.

( $N_{\text{BChl}}$  denotes the number of BChl in the complex). The counting of the levels starts with the excitonic energy  $\hbar\Omega_\alpha$  of lowest energy and ends at the highest-lying level. The two-exciton states follow as

$$|\tilde{\alpha}\rangle = \sum_{m,n} \tilde{C}_\alpha(m,n) |m e, n e\rangle + \sum_m \tilde{C}_\alpha(m) |m f\rangle \quad (2)$$

which includes the superposition of states  $|m e, n e\rangle$  with two  $Q_y$ -excitations at different BChl and of the states  $|m f\rangle$  with a single excitation in the higher-excited BChl state. The present description comprises  $N_{\text{BChl}}(N_{\text{BChl}} - 1)/2 + N_{\text{BChl}}$  two-exciton states; thus,  $\tilde{\alpha}$  runs from 1 to 28, again starting with the lowest-lying value of the two-exciton energies  $\hbar\tilde{\Omega}_{\tilde{\alpha}}$ . Respective MX transition-dipole matrix elements are not given here but can be found in Appendix A.

There are numerous attempts to determine the (single) exciton levels of the FMO complex. We use the site energies, dipole-dipole couplings, and overall strengths of the spectral densities (see below), according to the recent detailed analysis of Wendling et al.<sup>23</sup> Table 1 specifies the BChl site energies that have been used. The resulting squares of the single-exciton expansion coefficients are shown in Figure 2, indicating how different exciton states contribute to a localized excitation at BChl  $m$ . In Table 2, one may find the respective single-exciton energies  $\hbar\Omega_\alpha$  and dipole moments  $\mathbf{d}_\alpha$ . The delocalization numbers of the exciton states (inverse participation ratio,  $N_\alpha = 1/\sum_m |C_\alpha(m)|^4$ ) are also given in Table 2. All the mentioned data emphasize the fact that the energetically lowest exciton level is mainly concentrated on the single BChl  $m = 3$ . The other exciton levels are somewhat more delocalized, at least at two different BChl. In particular, there is a considerable alteration of transition-dipole moments when changing from those of the single chromophore to those of the exciton states (see eq A3 in

**TABLE 2: Square of Single-Exciton Dipole Moments ( $d_\alpha$ ), Their  $x$ -Component,<sup>a</sup> and the Respective Excitonic Energies, Together with Their Delocalization Number (Inverse Participation Ratio,  $N_\alpha$ )<sup>b</sup>**

$\alpha$	$ d_\alpha ^2$	$ d ^2$	excitonic energy, $\hbar\Omega_\alpha$		$N_\alpha$
			(cm <sup>-1</sup> )	(nm)	
1	0.64	0.66	12139	823.8	1.24
2	0.16	2.13	12290	813.7	1.78
3	0.01	0.95	12322	811.5	2.35
4	1.21	1.39	12426	804.7	2.02
5	0.61	1.21	12485	801.0	2.14
6	0.09	0.16	12535	797.8	2.25
7	0.07	0.50	12667	789.4	1.80

<sup>a</sup> In units of the square of a single  $Q_y$  dipole moment of 40 D<sup>2</sup> (see ref 23). <sup>b</sup> The  $x$ -direction is defined by the direction of the electric field strength.

**TABLE 3: Lifetime of the Different Excitonic States ( $\tau_\alpha$ )<sup>a</sup>**

$\alpha$	$\tau_\alpha$ (ps)		
	4 K	77 K	265 K
1	$\infty$	193	8.5
2	82	33	3.5
3	7.4	5.8	1.8
4	8.8	6.6	2.0
5	4.0	3.3	1.4
6	2.0	1.9	1.1
7	1.8	1.8	1.2

<sup>a</sup>  $\tau_\alpha = 1/\sum_\beta k(\alpha \rightarrow \beta)$ .

Appendix A). Therefore, we conclude that it is more appropriate to use a description with exciton states instead of an approach exclusively based on localized  $Q_y$ -excitations. In regard to the parameters of the two-exciton states, we proceed as explained above (see also our earlier analysis given in ref 22).

**II.B. MX Density Matrix Theory.** Using the MX states, which, in the general case, read  $|\alpha_N\rangle$  with  $N$  labeling the respective manifold (remember  $|\alpha_1\rangle = |\alpha\rangle$ ,  $|\alpha_2\rangle = |\tilde{\alpha}\rangle$ ), we may introduce the MX density matrix as

$$\rho(\alpha_M, \beta_N; t) = \langle \alpha_M | \hat{\rho}(t) | \beta_N \rangle \quad (3)$$

Here,  $\hat{\rho}(t)$  is the reduced MX density operator, which, in the present case, should obey the quantum master equation (cf. Appendix A). MX excitation energy dissipation and dephasing are originated by a coupling to intrachromophore vibrations as well as more delocalized interchromophore vibrations covering a portion of or the entire protein. The latter type of vibrations enters the quantum master equation via transition processes among MX states of the same manifold, accompanied by the emission or absorption of a single vibrational quantum.

The MX vibrational coupling are characterized by the MX spectral densities (see eq A7 of Appendix A). They can be related to spectral densities that describe the coupling to localized BChl excitations, as well as the interchromophore coupling.<sup>19</sup> We provide the existence of site-local vibrations, which only modulate the first excited state  $\varphi_e$  of the chromophores and do not influence the intersite electronic coupling. Because the lifetime of the  $\varphi_f$  state is strongly restricted by the internal conversion process (with  $\tau_{\text{IC}} = 35$  fs) to the  $\varphi_e$  state, there was no need to introduce an additional coupling to vibrational modes (finally, such an additional coupling would have no essential effect on the two-exciton dephasing). The used model with site-local vibrations results in a single spectral density  $J_e(\omega)$ .<sup>25</sup> The resulting single-exciton lifetimes are listed in Table 3. As expected, they decrease drastically as the

temperature increases. Moreover, the lifetimes decrease from the lower part to the upper part of the exciton level scheme, because the number of final states increases, in particular at low temperatures. In any case, all values that exclusively lie above 1 ps indicate that dissipation should influence the control task only moderately, provided that it has been performed with a pulse of subpicosecond duration.

Intrachromophore vibrations also may participate in the intramanifold MX scattering. However, they are also involved in the internal conversion process, because it is a part of EEA. Because our description is based on (delocalized or partially delocalized) MX states, EEA seems to be a nonradiative transition from a higher exciton manifold to a lower exciton manifold. For example, if the two-exciton state component  $\tilde{C}_{\tilde{\alpha}}(m)$  related to a double excitation of a single chromophore at site  $m$  (cf. eq 2) is nonzero, an internal conversion to the state  $\varphi_e$  of chromophore  $m$  will appear. The single-chromophore excitation may be the part of the single-exciton state  $|\beta\rangle$  with expansion coefficients  $C_{\beta}(m)$ . If the internal conversion is assumed to be fast, compared to all other processes of exciton motion, EEA can be taken into consideration in the quantum master equation via the rates  $k^{(EEA)}(\tilde{\alpha} \rightarrow \beta)$ . The rates are proportional to the internal conversion rate  $1/\tau_{IC}$  but also include MX wave function overlap expressions  $|\tilde{C}_{\tilde{\alpha}}(m)|^2|C_{\beta}(m)|^2$ , which may strongly reduce the value of  $1/\tau_{IC}$  (see ref 26 and Appendix A.2).

### III. Determination of the Optimal Pulse

This section shortly reviews the method of Optimal Control Theory (OCT).<sup>1,2,21</sup> It turns out to be an adequate tool for computing the laser pulse that drives the system in the required manner. We will call this pulse, which represents a solution of the OCT, the *optimal pulse*.

**III.A. Prologue.** Before applying the apparatus of OCT, let us try to answer, in a more direct way, the question whether a spatial localization of excitation energy is possible. To do this, we invert eq 1

$$|me\rangle = \sum_{\alpha} C_{\alpha}^{*}(m)|\alpha\rangle \quad (4)$$

and obtain a localized state via the superposition of all exciton states. If it would be possible to prepare such a superposition state by an optical transition, the entire excitation would seem to be localized at the  $m$ th chromophore (the target site,  $m_{\text{tar}}$ ).

Provided that there are weak excitation conditions, i.e., a description which is of first order in regard to the field strength, the excited superposition state in the single exciton manifold reads

$$|\Psi^{(1)}(t)\rangle = \sum_{\alpha} A_{\alpha}(t)|\alpha\rangle \quad (5)$$

The time-dependent expansion coefficients have the following form:

$$A_{\alpha}(t) = \frac{i}{\hbar} \int_{t_0}^t dt \exp[-i\Omega_{\alpha}(t - \bar{t})] d_{\alpha} E(\bar{t}) \rightarrow \frac{i}{\hbar} \exp(-i\Omega_{\alpha}t) d_{\alpha} E(\Omega_{\alpha}) \quad (6)$$

In the second part of this expression, we assumed that the actual time  $t$  is larger than  $t_f$ , the time at which  $E$  vanishes.

The expansion coefficients then are determined by the Fourier-transformed field pulse taken at the exciton frequencies  $\Omega_{\alpha}$ . To let  $|\Psi^{(1)}(t)\rangle$  (eq 5) be localized in the state  $|m_{\text{tar}}e\rangle$  (the target state) at time  $t_f$  (at the end of the pulse), we must identify (cf. eq 4)

$$C_{\alpha}^{*}(m_{\text{tar}}) = \frac{1}{\sqrt{\mathcal{N}}} A_{\alpha}(t_f) \quad (7)$$

Here, the amplitude  $A_{\alpha}(t)$  must be renormalized by  $\mathcal{N} = \sum_{\beta} |A_{\beta}(t)|^2$ , because the weak excitation condition allows  $\mathcal{N}$  to become much less than 1, whereas the exciton expansion coefficients are normalized to 1.

If the chromophore complexes are placed in a regular spatial arrangement, the orientation of the excitonic dipole moments, with respect to the polarization of the radiation field, determine the mutual coupling strength. For the computations, where we assumed such a regular arrangement of all FMO complexes, the field is polarized in the  $x$ -direction. Hence,  $A_{\alpha}$  from eq 6 becomes proportional to the  $x$ -component of  $d_{\alpha}$  (cf. Table 2; the different values indicate that it might be unfavorable to excite exciton levels 3, 6, and 7).

Noting eqs 6 and 7, we may determine the Fourier components of the field, which would drive the exciton wave function into the localized state. Needless to say, the computation of a time-dependent field by a discrete set of Fourier components (seven in the present case of the FMO complex) remains incomplete. Nevertheless, it seems reasonable to take the following ansatz:

$$\tilde{E}(t) = -i\hbar\sqrt{\mathcal{N}}f(t)e \sum_{\alpha} \exp[-i\Omega_{\alpha}(t - t_f)] \frac{C_{\alpha}^{*}(m_{\text{tar}})}{d_{\alpha}} + c.c. \quad (8)$$

Here,  $e$  is the polarization unit vector of the field pulse and we used the notation  $d_{\alpha} = ed_{\alpha}$ . The function  $f(t)$  is an envelope that guarantees that the pulse vanishes for  $t < t_0$  and  $t > t_f$ . It has been taken as a Gaussian function with a length of  $(t_f - t_0)/3$ . This choice ensures that the Fourier transform of eq 8 fulfills eq 7. We will call  $\tilde{E}(t)$  the approximate optimal field.

Of course, the disadvantage of the given reasoning lies in the restriction to low field intensities and the neglect of energy relaxation and dephasing. Nevertheless, it represents a straightforward way to discuss spatial energy localization and will be used in Section IV. Going to larger field intensities, we will apply the method of OCT, but, at the same time, it becomes necessary to include higher exciton manifolds, at least the two-exciton one.

**III.B. Optimal Control Theory.** Although it would be most appropriate to formulate the OCT in a way where a spectroscopic quantity (for example, a probe pulse absorption) is optimized,<sup>27</sup> here, we apply the standard formulation. It assumes a target state  $|\Psi_{\text{tar}}\rangle$  which should be reached at a certain time  $t_f$  (see, for example, refs 1, 2, and 21). In the present case, we set  $|\Psi_{\text{tar}}\rangle = |m_{\text{tar}}e\rangle$ , where  $m_{\text{tar}}$  denotes the site at which the  $Q_y$ -state of the respective BChl should be populated as much as possible. If one introduces the target operator

$$\hat{\Pi}_{\text{tar}} = |m_{\text{tar}}e\rangle\langle m_{\text{tar}}e| \quad (9)$$

the laser pulse control of molecular dynamics then can be formulated as the task to realize that the expectation value  $P_{\text{tar}}(t_f)$

of the target operator equals one at a certain final time  $t_f$ . This expectation value reads

$$\begin{aligned} P_{\text{tar}}(t_f) &= \text{tr}_{\text{MX}}\{\hat{\rho}(t_f)\hat{\Pi}_{\text{tar}}\} \\ &\equiv \langle m_{\text{tar}}e | \hat{\rho}(t_f) | m_{\text{tar}}e \rangle \\ &= \sum_{\alpha, \beta} C_{\alpha}(m_{\text{tar}}) C_{\beta}^*(m_{\text{tar}}) \rho(\alpha, \beta; t_f) \end{aligned} \quad (10)$$

Here,  $\text{tr}_{\text{MX}}$  denotes the trace, with respect to the MX states, under consideration and  $\hat{\rho}$  is the MX density operator introduced in eq 3.

To reach  $P_{\text{tar}}(t_f) = 1$ , the applied field pulse  $\mathbf{E}(t)$  should drive the MX system in the required manner. As a rule, what would be reachable is not  $P_{\text{tar}}(t_f) = 1$  but  $P_{\text{tar}}(t_f)$  equal to a value somewhat less than 1. The laser pulse that realizes this extremum of  $P_{\text{tar}}(t_f)$  represents the optimal pulse. If a constraint is introduced to guarantee a finite field strength, the optimal pulse follows as the extremum of the following functional:

$$J(t_f; \mathbf{E}) = P_{\text{tar}}(t_f; \mathbf{E}) - \frac{1}{2} \int_{t_0}^{t_f} dt \frac{E^2(t)}{\lambda \Lambda_0 f(t)} \quad (11)$$

The penalty factor  $\lambda \Lambda_0$  has been combined with the function  $f(t)$  (introduced in the previous subsection), which avoids a sudden switch on and switch off of the control field. The quantity  $\lambda$  is dimensionless and will vary between 0 and 1, whereas  $\Lambda_0$  is equal to  $1 \text{ eV}/d_{\text{BChl}}^2$  (the quantity  $d_{\text{BChl}}$  is the  $Q_y$ -transition dipole moment introduced in Section II.A). Although the constraint in eq 11 guarantees finite pulse intensity, this intensity must be determined after the optimal pulse has been computed (it becomes a function of the given penalty factor).

In Appendix B, some details are given in regard to how to determine the extremum of  $J(t_f; \mathbf{E})$ . Here, we only shortly comment on the procedure. In a first step, one must compute the functional derivative of  $J(t_f; \mathbf{E})$ . The demand that the derivative equals zero results in a nonlinear functional equation of the type  $\mathbf{E}(t) = \lambda \Lambda_0 f(t) \mathbf{K}(t_f, t; \mathbf{E})$ , where  $\mathbf{K}(t_f, t; \mathbf{E})$  is the so-called control kernel. Its value at time  $t$  can be determined by a forward propagation of  $\hat{\rho}$  from  $t_0$  to  $t$  and a backward propagation of an auxiliary density operator  $\hat{\delta}$  from  $t_f$  to  $t$ . The coupling of both density operator propagations by the field and, thus, by the control kernel allows the introduction of an efficient iteration scheme to determine the optimal pulse (for details, see Appendix B and refs 12–14).

The given formulations are intended for a complete population of the target state. In the present case, this means that every FMO complex in the sample has the chosen BChl in its  $Q_y$ -state. (In the experiment, such a complete excitation requires intensities at which the neglect of higher exciton manifolds is no longer justified.) To determine optimal pulses, which only lead to a weak overall excitation of the sample, we set, for the target operator,

$$\hat{\Pi}_{\text{tar}} = (1 - x) |0\rangle\langle 0| + x |m_{\text{tar}}e\rangle\langle m_{\text{tar}}e| \quad (12)$$

It describes a mixture of the ground state  $|0\rangle$  and the presence of a single excited state, the target state  $|m_{\text{tar}}e\rangle$ . The presence of the latter in the mixture is regulated by  $x$  (the mixing parameter). If  $x$  is taken to be very small, the population of the target state also should become small (the excitation of other BChl is totally suppressed). In contrast, for  $x = 1$ , we arrive again at the target operator described in eq 9.

## IV. Numerical Results

As already indicated in the previous sections, our discussion will concentrate on laser pulse localization of excitation energy. We will start with the case where higher manifolds than the single-exciton one, as well as the influence of orientational and structural disorder, are neglected.

**IV.A. Influence of Dissipation.** We provide a completely ordered ensemble of FMO complexes with the  $x$ -component of the exciton transition-dipole matrix element coupling to the electric field strength of the linearly polarized laser pulse (cf. Table 2). To analyze the localization of the excitation energy, we study its dependence on the length of the control pulse ( $\tau_c$ ) and on temperature. According to the formulation of the OCT in the preceding section, the pulse length  $\tau_c$  is given by  $t_f - t_0$ , and, in this way, we may consider a dependence of the solution of the control task on the final time. Figure 3 shows the obtained results for some selected BChl of the FMO complex ( $m_{\text{tar}} = 3, 4, \text{ and } 7$ ), at three temperatures as well as in the dissipationless case. It is drawn the population of the  $Q_y$ -state of one of the seven BChl (the target state) versus  $\tau_c$ . This time varies between 200 and 1200 fs, in steps of 200 fs. The given values for the site populations are the result of 50 iterations of the forward and backward propagations (cf. Appendix B).

The calculations presented in Figure 3 must be considered as reference calculations for the subsequent discussion. They try to achieve a complete population of the target state  $|m_{\text{tar}}e\rangle$ . The population difference between  $P_{\text{tar}}(t_f)$  and 1 may be distributed among other singly excited BChl as well as the ground state (probability conservation in the absence of two-exciton states read  $1 = P_0 + \sum_{\alpha} P_{\alpha}$ ). We will return to this point of discussion later.

As expected, the achieved population of the target state decreases as the temperature increases and increases as the pulse length increases. The behavior is typical for all shown control tasks. However, the achieved total population of the target state is dependent on the chosen BChl at which excitation energy should be localized. At 4 K, the excitation of BChl  $m = 4$  as well as  $m = 2, 5$  (not shown) remains  $< 0.6$ . This result can be explained by the magnitude of the excitonic dipole matrix elements (their component showing in the polarization of the laser pulse). According to Table 2, exciton levels 3, 6, and 7 have the smallest values. As can be directly deduced from Figure 2, just those exciton levels dominate the excitonic wave packet (eq 4) just for  $m = 2, 4, \text{ and } 5$ . Moreover, an inspection of Figure 3 shows that the population of BChl  $m = 3$  stays constant after  $\tau_c$  has overcome a value of 400 ps. This behavior can be explained by the dominance of BChl  $m = 3$  by the lowest exciton level (cf. Figure 2). To excite  $m = 3$ , it is sufficient to excite the exciton level  $\alpha = 1$ . The decrease of the target state population with increasing temperature results from the fact that excitonic energy relaxation and dephasing increases their influence when temperature becomes greater. Such an increase of dissipative effects acts counterproductive to the external field, which tries to form a spatially localized wave packet at  $t = t_f$ . Of course, the details of these dissipative effects are dependent on the concrete environment of the BChl and the strength it couples to the surrounding BChl (cf. Section II).

The way the target state population increases as the length of the control pulse ( $\tau_c$ ) increases is different for different BChl; however, first of all, it does reflect the fact that an increase of  $\tau_c$  offers the possibility to concentrate more probability in the target state. However, if  $\tau_c$  becomes too large, the excitonic wave packet forming the localized state decays during its formation, because of dissipative effects. This explains the final

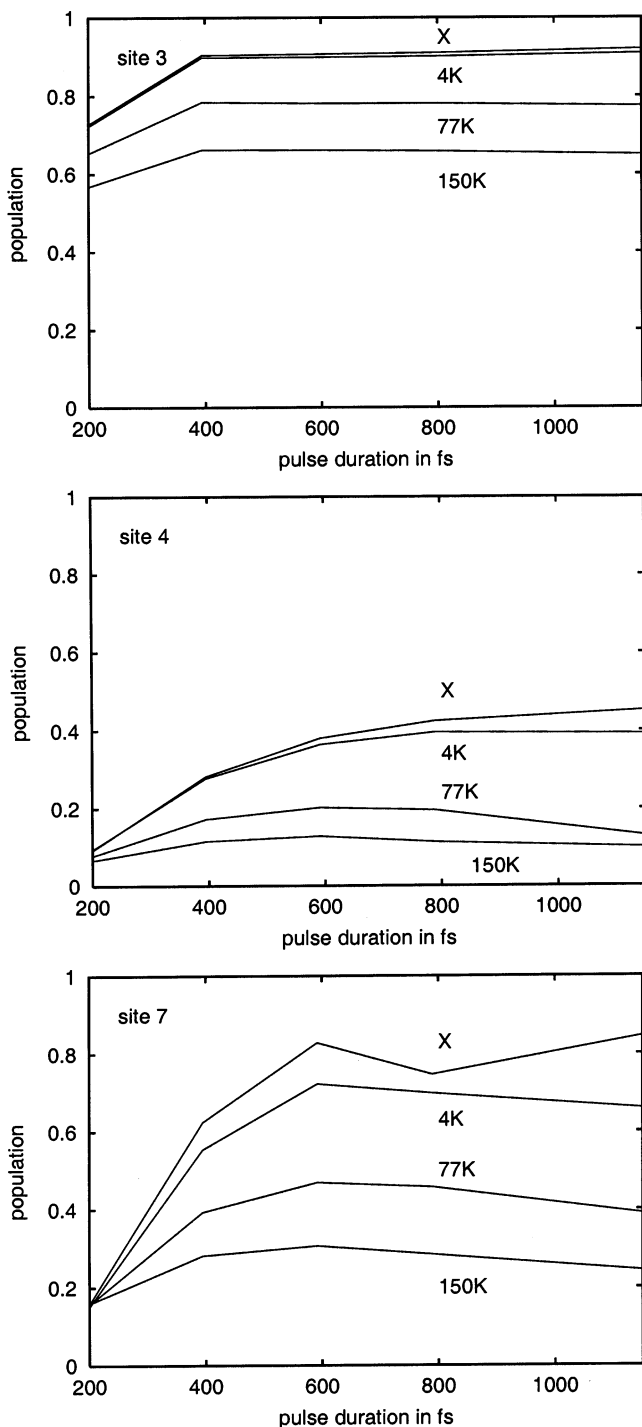


**Figure 3.** Population of single BChl  $Q_y$ -states (target states) after an excitation with the respective optimal pulse (at  $t_f$ ), drawn versus the duration  $\tau_c$  of the optimal pulse. Upper panel: target states  $m_{\text{tar}} = 3$ ; middle panel:  $m_{\text{tar}} = 4$ ; lower panel:  $m_{\text{tar}} = 7$  (the populations for  $m_{\text{tar}} = 1, 2, 5$ , and  $6$  behave similar to those of  $m_{\text{tar}} = 7$ ). Curves are shown for different temperatures. Populations calculated at the absence of dissipation are marked with a  $\langle x \rangle$ . Up to 50 iterations have been used. The penalty factor ( $\lambda$ ) has been set equal to 0.25.

decrease of the target population with increasing  $\tau_c$ . In conclusion, we will use a control pulse length of  $\tau_c \approx 600$  fs, which is most adapted to the considered MX dynamics and, thus, leads to the largest control yield.

In our further discussions, we will mainly concentrate on the excitation energy localization at the  $m = 7$  BChl (cf. Figure 1). According to Figure 2, it is formed by the contributions of different exciton levels, with level 5 dominating the super-

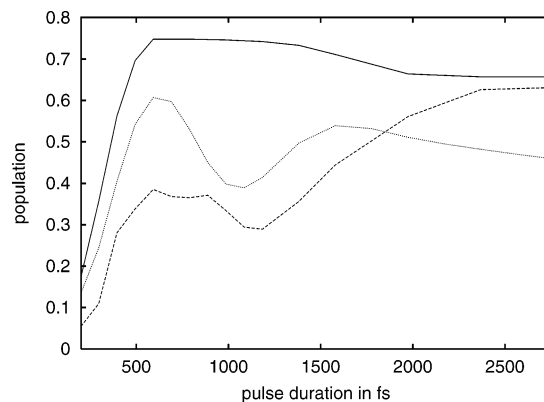


**Figure 4.** Renormalized population (eq 13) of the target state  $m_{\text{tar}} = 7$  versus the duration  $\tau_c$  of the pulse after excitation with an optimal pulse (up to 2000 iterations have been performed) (denoted by the solid line), after excitation with a Gaussian pulse (denoted by the dotted line), and after excitation with the approximate optimal pulse (eq 8) (denoted by the thin solid line) (we took  $T = 4$  K and  $\lambda = 0.25$  for all curves, the Gaussian and the approximate optimal pulse lead only to a small population of the excited states, whereas for the optimal pulse the ground state is almost empty).

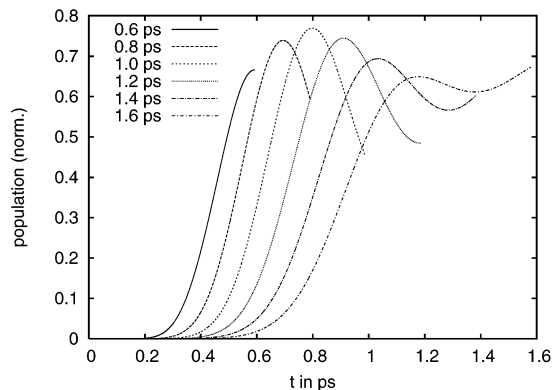
position state. To compare the results shown in Figure 3 with the case of weak excitation, we introduce the renormalized population

$$p_{\text{tar}}^{(\text{ren})}(t_f) = \frac{P_{\text{tar}}(t_f)}{\sum_{\alpha} P_{\alpha}(t_f)} \equiv \frac{P_{\text{tar}}(t_f)}{1 - P_0(t_f)} \quad (13)$$

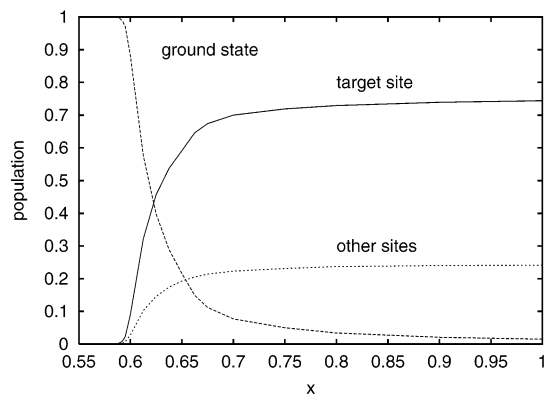
It measures the excitation energy localization in relation to the total excitation into the single-exciton manifold and, consequently, represents a quantity (somewhat) independent of the actual degree of excitation.

Figure 4 compares  $p_{\text{tar}}^{(\text{ren})}(t_f)$ , which has been drawn versus  $\tau_c$ , with the reduced population achieved by a Gaussian pulse and the ansatz for the control field, according to eq 8. First of all, we can state that the pulse determined by the OCT leads to the best spatial excitation energy localization lying above 0.75. The field pulse according to eq 8 reaches this result only for large pulse durations. The Gaussian pulse applied with a carrier frequency of  $\omega = \Omega_{\alpha=5}$  never achieves a renormalized population of  $>0.6$ . This demonstrates (in a somewhat indirect way) the complexity of the control pulse. It is neither a single Gaussian nor a simple combination of Gaussian pulses, such as that in eq 8. A similar behavior can be found for the absence of dissipation but with an overall larger control yield (not shown). To understand the minimum of the target state population obtained when a Gaussian-shaped pulse or the pulse according to eq 8 is applied, Figure 5 displays the target-state population versus time up to the actual value of  $t_f$  for the Gaussian-shaped pulse. As it becomes obvious, destructive interferences in the excitonic wave packet decrease the target-state population within a certain range of  $t_f$ . This explains the large depression observed in Figure 4.

Figure 6 gives a different view on the optimal-pulse-driven population dynamics drawn in Figure 3. We chose the case  $\tau_c = 600$  fs (and  $T = 4$  K), because it is best adapted to an efficient control of the MX dynamics. One may observe a total redistribution of population from the FMO ground state  $|0\rangle$  into the target state, as well as all other  $Q_y$ -states. Because Figure 6 displays the results of computations for the type of mixed target state, defined in eq 12, first one must concentrate on the case



**Figure 5.** Renormalized population (eq 13) of the target state  $m_{\text{tar}} = 7$  versus time for a Gaussian pulse of different length and for the absence of dissipation (note that the populations have been only drawn up to the respective  $t_f$ , and, furthermore, that we used a value of  $\lambda = 0.25$ ).



**Figure 6.** Population of the target site  $m_{\text{tar}} = 7$  of the ground state and of the sum over all other site populations versus the mixing parameter introduced in eq 12 (the target state is a linear combination of the ground state and the state, where only BChl 7 is excited). The pulse duration was 600 fs,  $T = 4$  K, and  $\lambda = 0.25$  (the renormalized target state population (eq 13) stays at the value of 0.76 over the entire  $x$ -range).

$x = 1$ . Here, more than 70% of the excited state population is concentrated in the target state. This condition is valid for a case of almost-complete ground-state depletion. If  $x$  is reduced, the target-state population remains almost constant until  $x$  decreases below a value of 0.7. However, the reduced target-state population (eq 13) remains at 0.76 over the entire range of  $x$  (not shown).

**IV.B. Influence of Two-Exciton States and Disorder.** Let us turn to the inclusion of two-exciton states (eq 2). We expect two additional effects when compared with a description including single-exciton states only. First, it is unavoidable to create a wave packet in the two-exciton manifold beside that in the single-exciton manifold. Both wave packets are driven simultaneously by the control pulse but must be reduced to a single-exciton wave packet at  $t = t_f$  by stimulated recombination from the two-exciton manifold. Second, the entire dynamics includes a new relaxation channel: the EEA from the two-exciton manifold to the single-exciton manifold, which would strongly affect the driven (coherent) two-exciton to single-exciton transition. In conclusion, we should obtain a reduced control yield.

Details of the temporal-state population, together with the optimal pulse, are shown in Figure 7. We used the same parameters as in Figure 6 ( $t_f = 600$  fs). The optimal pulse consists of two sub-pulses, the later one with a tail extending up to  $t = 500$  fs. It becomes obvious from a comparison of the

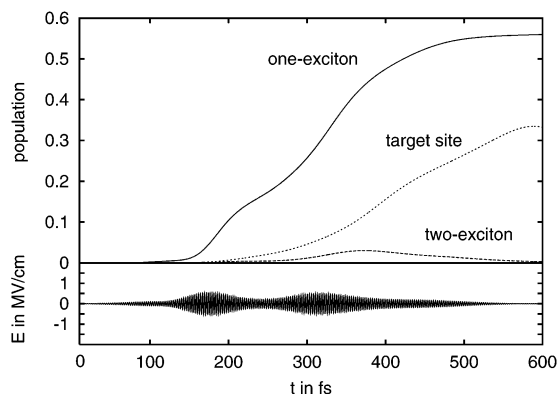


**Figure 7.** Population of the target site  $m_{\text{tar}} = 7$  versus time, together with the optimal pulse in the lower panel, the pulse duration is 600 fs,  $T = 4$  K, the mixing parameter is  $x = 1$ , and  $\lambda = 0.25$ .

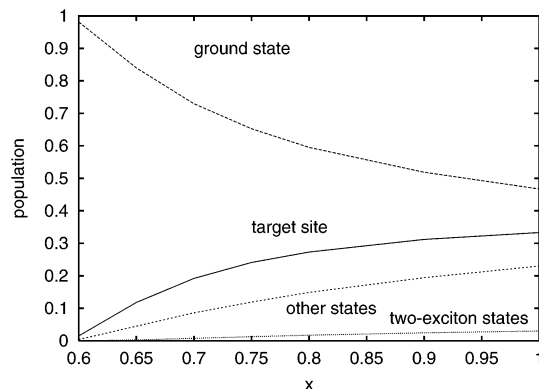


**Figure 8.** Populations including the two-exciton states versus the mixing parameter introduced in eq 12 (the target state is a linear combination of the ground state and the state, where only BChl 7 is excited); the pulse duration was 600 fs,  $T = 4$  K, and  $\lambda = 0.25$  (the renormalized target-state population; eq 13 decreases from 0.76 at  $x = 0.6$  to 0.59 at  $x = 1.0$ ).

total single-exciton population with the target population that the first sub-pulse mainly results in overall population of the singly excited states different from the target state. The population of the target state is achieved by the second sub-pulse, which increases the amplitudes of the single-exciton states (which is consistent with an increase of the total single-exciton population). The respective tail between 400 and 500 fs allows the wave packet to move into the target state. Simultaneously, an intermediate two-exciton state population appears. Because of EEA and stimulated recombination, however, this population is strongly decreased at  $t = t_f$ .

To compare the control yield at the presence of two-exciton states with that at their absence, we have repeated the calculations leading to Figure 6. For the mixed target state used (eq 12), we expect a small mixing parameter  $x$  to be particularly important for a suppression of the dominance of two-exciton states. Respective results can be found in Figure 8. Indeed, the largest ratio between the target-state population ( $m_{\text{tar}} = 7$ ) and the total population of the single exciton manifold  $p_{\text{tar}}^{(\text{ren})}(t_f)$  (eq 13) is obtained for a modest total excitation ( $x = 0.6$ ). The ratio  $p_{\text{tar}}^{(\text{ren})}(t_f)$  reaches 0.76 but decreases to a value of 0.59 at  $x = 1$ . Incidentally, this is in contrast to Figure 6, where  $p_{\text{tar}}^{(\text{ren})}(t_f) = 0.76$  for all  $x$ . Moreover, the inclusion of two-exciton states leads to a ground-state depletion of  $P_0 = 0.47$  at  $x = 1$ , and the total two-exciton state population  $\sum_{\alpha} \rho_{\alpha\alpha}(t_f)$  remains small. Note that Figure 8 shows the maximal two-exciton population and not the population present at  $t_f$ . The latter is strongly decreased by exciton exciton annihilation processes (cf. Figure 7).

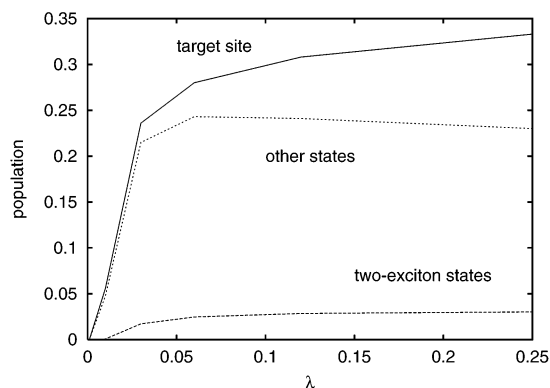


**Figure 9.** Simulation of the populations including the two-exciton states and that of the target site  $m_{\text{tar}} = 7$  in dependency on the penalty factor  $\lambda$  (for a pulse duration of 600 fs and  $T = 4$  K, the renormalized target state population (eq 13) increases from 0.51 at  $\lambda = 0.03$  to 0.59 at  $\lambda = 0.25$ ).

Although the data of Figure 8 have been calculated for the same parameters as those shown in Figure 6, except the inclusion of two-exciton states, the results differ remarkably. While, in Figure 6, the ground state is almost completely depopulated for larger values of the mixing parameter  $x$ , this is not the case when transitions into two-exciton states become possible. In this case, according to the chosen target state, OCT tries to reduce the two-exciton populations as much as possible but in accepting a much smaller target-state population. The population of the target state is further influenced by dissipation that is associated with EEA, which also hinders coherent single-exciton wave packet formation.

The way this population is dependent on the penalty factor  $\lambda$  (cf. eq 11) has been discussed in Figure 9 (for the case of  $x = 1$ ). As expected, an increasing  $\lambda$  value initiates an increase of the overall field strength of the optimal and, thus, of the population of the target state. Interestingly, this is accompanied by an decrease of the site population of all other BChl as well as a very weak increase of the two-exciton population (again, the maximal population is shown and not that at  $t_f$ ). All the given results demonstrate that laser pulse localization of the exciton energy becomes possible, even if higher exciton manifolds are discussed.

At the end of our discussion, we will investigate the influence of energetic and structural disorder. The presence of disorder results in the fact that the optimal pulse is determined as a compromise, with respect to all the driven FMO dynamics, differing somewhat from complex to complex in the probe volume. As a result, the optimal pulse must be obtained from a particular disorder average (see also Appendix B.2). Because this represents a computational, very expensive task, the reported data are of preliminary and oriented character. Only a restricted number of disorder configurations could be included and it became necessary to neglect the two-exciton states. Some results are shown in Figure 10, where the disorder-averaged population of the target state has been drawn versus the time up to  $t_f$ . The considered types of disorder include random orientation of the single FMO complexes in space and a Gaussian distribution of the BChl site energies (diagonal disorder). As expected, disorder decreases the target-state population. However, this influence does not completely alter the results. A sufficiently large population of the target state (two times larger than all other state populations) becomes possible, independent of the actual number of configurations.

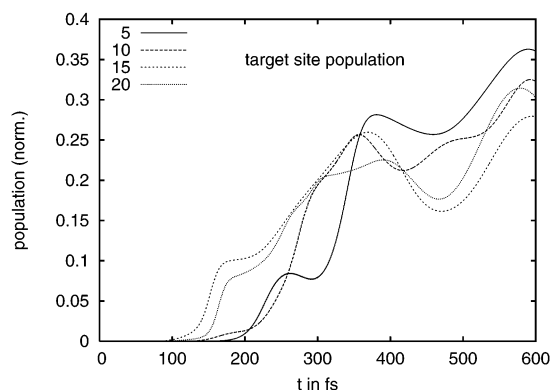


**Figure 10.** Effect of disorder (random orientations of the complexes and Gaussian diagonal disorder of the site energies of a full width at half maximum (fwhm) of  $100 \text{ cm}^{-1}$ ) on the renormalized population, eq 13 of the target state  $m_{\text{tar}} = 7$  versus time (optimal pulse of 600 fs duration,  $T = 4$  K, a mixing parameter  $x = 1$ , and  $\lambda = 0.25$ ). Calculations have been done for 5, 10, 15, and 20 disorder realizations.

## V. Conclusions

The present paper has reported on simulations that have been performed to demonstrate the possibility of guiding and localizing excitation energy in chromophore complexes by tailored femtosecond laser pulses. If a wave packet has been formed via the population of exciton states, the exciting laser pulse should drive this wave packet into such a form that it corresponds to a spatially local excitation of a single chromophore. To exemplify the idea, the FMO complex of green sulfur bacteria has been chosen. It represents a well-characterized pigment–protein complex with seven Bacteriochlorophyll (BChl) molecules in its monomeric form, with the presence of (partially) delocalized exciton states, and with a proper distribution of oscillator strength across the exciton states (necessary for a flexible wave packet formation).

The possibility has been tested to populate a single  $Q_y$ -state of one of the seven BChl of the FMO complex. Even under realistic conditions, such as the inclusion of two-exciton states and the influence of energy relaxation and dephasing, such a spatial localization of excitation energy is possible within a time interval of some hundreds of femtoseconds and with a sufficient large yield. Some preliminary attempts to include structural and energetic disorder have also been made.

Our description has been based on the standard version of optimal control theory by assuming a target state to be reached at a particular time. To overcome this restrictive description, we demonstrated recently how to optimize the probe pulse absorption in a pump–probe scheme,<sup>27</sup> which also might represent a successful experimental approach for the example studied here. It would be also of interest to translate the given simulation to larger chromophore complexes, such as the core–antenna system PS1. Such investigations are in progress.<sup>28</sup>

**Acknowledgment.** Financial support by the Sonderforschungsbereich 450 (DFG, Germany) is gratefully acknowledged.

## Appendix A. Multiexciton Density Matrix Theory

In the following, the main ideas of the MX density matrix theory are shortly reviewed. For more details, we refer the reader to refs 19 and 20.

**A.1. Multiexciton States.** MX states  $|\alpha_N\rangle$  represent the electronic *eigenstates* of interest for the considered type of

chromophore complex. The number  $N$  in the MX quantum number  $\alpha_N$  indicates the respective manifold (single-exciton manifold, two-exciton manifold, etc.). MX states appear as superposition states of locally excited states  $|\{m e, n f\}_N\rangle$  according to

$$|\alpha_N\rangle = \sum_{\{m e, n f\}_N} C_{\alpha_N}(\{m e, n f\}_N) |\{m e, n f\}_N\rangle \quad (\text{A1})$$

This notation represents a generalization of eqs 1 and 2 for the single-exciton and two-exciton states, respectively. The states  $|\{m e, n f\}_N\rangle$  refer to an  $N$ -fold excitation of the chromophore complex, with the molecules at sites  $m_1, \dots, m_M$  in the first excited state ( $\varphi_e$ ) and the molecules at sites  $n_1, \dots, n_N$  in the higher state ( $\varphi_f$ ). When performing the summation in eq A1, the numbers  $M$  and  $N$  are related to  $N$  by the condition  $N = M + 2N$ . Of course, the notation with an arbitrary  $N$  is of less importance here, because the concrete computations are restricted to the incorporation of the two-exciton manifold only.

The MX states described in eq A1 can be used to introduce the MX representation of the entire Hamiltonian (cf. ref 20).

$$H = \sum_N \left( \sum_{\alpha_N} \hbar \Omega(\alpha_N) |\alpha_N\rangle \langle \alpha_N| + \sum_{\alpha_N \beta_N} H_{\text{vib}}(\alpha_N, \beta_N) |\alpha_N\rangle \langle \beta_N| + \sum_{N>1} \sum_{\alpha_{N-1}, \beta_N} [\Theta(\alpha_{N-1}, \beta_N) |\alpha_{N-1}\rangle \langle \beta_N| + \text{h.c.}] - E(t) \sum_N \sum_{\alpha_{N+1}, \beta_N} (d(\alpha_{N+1}, \beta_N) |\alpha_{N+1}\rangle \langle \beta_N| + \text{h.c.}) \right) \quad (\text{A2})$$

The first term describes free MX dynamics. The quantities  $H_{\text{vib}}(\alpha_N, \beta_N)$  are responsible for diagonal as well as off-diagonal MX-state coupling to localized intrachromophore vibrations and delocalized vibrations of the entire system. The third term on the right-hand side of eq A2 characterizes the intermanifold coupling originated by the nonadiabatic coupling between the higher excited state ( $\varphi_f$ ) and the first excited state ( $\varphi_e$ ). Optical transitions between different exciton manifolds are taken into consideration using the last term in eq A2, where  $E$  denotes the electric field strength.

The transition-dipole operator of the entire complex accounts for transitions from the BChl ground state ( $\varphi_g$ ) to the state ( $\varphi_e$ ), as well as from the latter one to the higher-excited state ( $\varphi_f$ ). This results in the following transition matrix elements from the ground-state into the single-exciton manifold (note the use of  $\alpha$  instead of  $\alpha_1$ , cf. Section II):

$$d_\alpha = \sum_m d_m(eg) C_\alpha^*(m) \quad (\text{A3})$$

The BChl  $Q_y$ -transition matrix elements  $d_m(eg)$  have been introduced in Section III. For the transition from the single-exciton state  $|\beta\rangle$  to the two-exciton state  $|\tilde{\alpha}\rangle$ , we get (note the use of  $\tilde{\alpha}$  instead of  $\alpha_2$ )

$$d_{\tilde{\alpha}\beta} = \sum_m \sum_{n \neq m} d_m(eg) C_{\tilde{\alpha}}^*(m, n) C_\beta(n) + \sum_m d_m(fe) C_{\tilde{\alpha}}^*(m) C_\beta(m) \quad (\text{A4})$$

**A.2. Density Matrix Equations.** The response to an optical excitation can be described by the MX density matrix (eq 3). For the systems of interest, it suffices to calculate the MX density matrix by means of an equation of motion, which is often called the quantum master equation or the multilevel

Redfield equation (see, for example, refs 19 and 21). This equation reads for the reduced MX density operator  $\hat{\rho}(t)$  as

$$\frac{\partial}{\partial t} \hat{\rho}(t) = -i(\mathcal{L}_{\text{mx}} + \mathcal{L}_{\text{field}}(t)) \hat{\rho}(t) - (\mathcal{R}_{\text{mx-vib}} + \mathcal{R}_{\text{EEA}}) \hat{\rho}(t) \quad (\text{A5})$$

The Liouville superoperator  $\mathcal{L}_{\text{mx}}$  denotes the commutator with the MX part  $\sum_{N, \alpha_N} \hbar \Omega(\alpha_N) |\alpha_N\rangle \langle \alpha_N|$  of  $H$  (see eq A2). The commutator with the field-dependent part of  $H$  is abbreviated by  $\mathcal{L}_{\text{field}}$ . MX energy relaxation, EEA, and dephasing are taken into consideration by the superoperator  $\mathcal{R}_{\text{mx-vib}} + \mathcal{R}_{\text{EEA}}$ . As is well-known, such a treatment provides a sufficient weak MX-vibration coupling. If a version of this approach is taken where any coupling between coherences and populations induced by the dissipative action of the vibrational DOF have been removed (secular approximation and Bloch model),  $\mathcal{R}_{\text{mx-vib}}$  and  $\mathcal{R}_{\text{EEA}}$  can be taken in the so-called Lindblad form.<sup>21,24</sup>

The contributions caused by the coupling to (intermolecular) vibrations read

$$\mathcal{R}_{\text{mx-vib}} \hat{\rho}(t) = \sum_N \sum_{\alpha_N, \beta_N} k^{(\text{mx-vib})}(\alpha_N \rightarrow \beta_N) \times \left\{ \frac{1}{2} [|\alpha_N\rangle \langle \alpha_N|, \hat{\rho}(t)]_+ - |\beta_N\rangle \langle \alpha_N| \hat{\rho}(t) |\alpha_N\rangle \langle \beta_N| \right\} \quad (\text{A6})$$

The intramanifold transition rates  $k^{(\text{mx-vib})}$  have been discussed in refs 19 and 20 and can be denoted as

$$k^{(\text{mx-vib})}(\alpha_N \rightarrow \beta_N) = 2\pi \Omega^2(\beta_N, \alpha_N) (1 + n(\Omega(\beta_N, \alpha_N))) \times (\mathcal{A}(\alpha_N \beta_N, \beta_N \alpha_N; \Omega(\beta_N, \alpha_N)) - \mathcal{A}(\alpha_N \beta_N, \beta_N \alpha_N; -\Omega(\beta_N, \alpha_N))) \quad (\text{A7})$$

Here, we have introduced  $\Omega(\beta_N, \alpha_N) = \Omega(\beta_N) - \Omega(\alpha_N)$  and  $n$  denotes the Bose-Einstein distribution.

The single-exciton spectral density and the two-exciton one, both entering the relaxation rate (eq A7) are taken as

$$\mathcal{A}(\alpha\beta, \beta\alpha; \omega) = \sum_m |C_\alpha(m) C_\beta(m)|^2 \times J_e(\omega) \quad (\text{A8})$$

and as

$$\mathcal{A}(\tilde{\alpha}\beta, \beta\tilde{\alpha}; \omega) = \sum_k \sum_{m \neq k, n \neq k} \tilde{C}_{\tilde{\alpha}}^*(k, m) \tilde{C}_\beta^*(k, m) \times \tilde{C}_{\tilde{\beta}}^*(k, n) \tilde{C}_{\tilde{\alpha}}(k, n) J_e(\omega) \quad (\text{A9})$$

In the case of EEA, it suffices to concentrate only on transitions from higher to lower manifolds, because the reverse processes are strongly unfavorable, in regard to energy. Accordingly, we have

$$\mathcal{R}_{\text{EEA}} \hat{\rho}(t) = \sum_N \sum_{\alpha_N, \beta_{N-1}} k^{(\text{EEA})}(\alpha_N \rightarrow \beta_{N-1}) \times \left\{ \frac{1}{2} [|\alpha_N\rangle \langle \alpha_N|, \hat{\rho}(t)]_+ - |\beta_{N-1}\rangle \langle \alpha_N| \hat{\rho}(t) |\alpha_N\rangle \langle \beta_{N-1}| \right\} \quad (\text{A10})$$

As shown in ref 20, the EEA rate for the transition from the two-exciton state  $|\tilde{\alpha}\rangle$  to the single-exciton state  $|\beta\rangle$  can be written as

$$k^{(\text{EEA})}(\tilde{\alpha} \rightarrow \beta) = \sum_m |C_{\tilde{\alpha}}(m)|^2 |C_\beta(m)|^2 k_{f \rightarrow e}^{(\text{IC})} \quad (\text{A11})$$

It contains the single chromophore internal conversion rate  $k_{f \rightarrow e}^{(\text{IC})}$  times the overlap between the probability to have a

double excitation at a certain chromophore and the probability to have a singly excited chromophore. Because the molecular internal conversion rate  $k_{f \rightarrow e}^{(IC)}$  enters eq A11, any modification of this nonadiabatic transition by excitonic effects has been neglected (cf. ref 20). However, excitonic effects enter the entire expression  $k^{(EEA)}$  for the EEA rate. The probability overlap in eq A11 indicates that EEA requires a two-exciton state  $|\tilde{\alpha}\rangle$  with a sufficient large probability to realize the excitation of the state  $\varphi_f$  at a certain chromophore. If the probability is also large to have the same chromophore in a single-exciton state  $|\beta\rangle$ , then the entire transition from  $|\tilde{\alpha}\rangle$  to  $|\beta\rangle$  becomes large.

The approach used in, e.g., by Ryzhov et al.,<sup>29</sup> where the transition from two spatially separated excitations to a double excited state has been described in perturbation theory, is also included in the present description. This becomes obvious by expanding  $|\tilde{C}_{\tilde{\alpha}}(mf)|^2$ , with respect to the related dipole–dipole coupling (for more details, see ref 19).

## Appendix B. Computation of the Optimal Pulse

**B.1. Absence of Disorder.** The extremum of the functional in eq 11, and, thus, the optimal pulse, is determined by the solution of the following equation:

$$\mathbf{E}(t) = \lambda \Lambda_0 f(t) \mathbf{K}(t_f, t; \mathbf{E}) \quad (\text{B1})$$

The so-called control kernel reads as

$$\mathbf{K}(t_f, t; \mathbf{E}) = \frac{i}{\hbar} \text{tr}_{\text{mx}} \{ \sigma(t) [\hat{\mu}, \hat{\rho}(t)]_- \} \quad (\text{B2})$$

It contains the propagation of the MX density operator  $\hat{\rho}$  from the initial time up to the intermediate time and a backward propagation of  $\hat{\sigma}$  from  $t_f$  to  $t$ . The latter propagation concerns the auxiliary density operator  $\hat{\sigma}(t)$  with  $\hat{\sigma}(t_f) = \hat{\Pi}_{\text{tar}}$ . According to refs 12 and 13, the equation of motion for  $\hat{\sigma}$  reads

$$\frac{\partial}{\partial t} \hat{\sigma}(t) = i(\mathcal{L}_{\text{mol}} + i\mathcal{L}_{\text{field}}(t))\hat{\sigma}(t) + (\tilde{\mathcal{R}}_{\text{mx-vib}} + \tilde{\mathcal{R}}_{\text{EEA}})\hat{\sigma}(t) \quad (\text{B3})$$

with the dissipative part

$$\tilde{\mathcal{R}}_{\text{mx-vib}} \hat{\sigma}(t) = \sum_N \sum_{\alpha_N, \beta_N} k^{(\text{mx-pro})}(\alpha_N \rightarrow \beta_N) \times \left\{ \frac{1}{2} [|\alpha_N\rangle\langle\alpha_N|, \hat{\sigma}(t)]_+ - |\alpha_N\rangle\langle\beta_N| \hat{\sigma}(t) |\beta_N\rangle\langle\alpha_N| \right\} \quad (\text{B4})$$

and

$$\tilde{\mathcal{R}}_{\text{EEA}} \hat{\sigma}(t) = \sum_N \sum_{\alpha_N, \beta_{N-1}} k^{(\text{EEA})}(\alpha_N \rightarrow \beta_{N-1}) \times \left\{ \frac{1}{2} [|\alpha_N\rangle\langle\alpha_N|, \hat{\sigma}(t)]_+ - |\alpha_N\rangle\langle\beta_{N-1}| \hat{\sigma}(t) |\beta_{N-1}\rangle\langle\alpha_N| \right\} \quad (\text{B5})$$

Both dissipative superoperators of the reverse propagation differ from the original one, with respect to their second term (the so-called sandwich term).

The two time-dependent density operators  $\hat{\rho}$  and  $\hat{\sigma}$  are coupled via the optimal pulse  $\mathbf{E}(t)$  entering  $\mathcal{L}_{\text{field}}(t)$ . To determine both density operators, we apply the iteration procedure suggested in ref 14. Therefore, one replaces  $\mathbf{E}(t)$  in  $\mathcal{L}_{\text{field}}(t)$  by eq B1 with the control kernel according to eq B2. The latter expression leads to a coupling between the equations of motion for  $\hat{\rho}$  and

for  $\hat{\sigma}$  by nonlinearities replacing the field term. In the case of the equation for  $\hat{\rho}$ , this term is dependent quadratically on  $\hat{\rho}$  but also linearly on  $\hat{\sigma}$ . In solving the equation, one needs an approximation for  $\hat{\sigma}$ . If the full time dependence of  $\hat{\rho}$  is known, one can determine  $\hat{\sigma}$  from  $t_f$  back to  $t_0$ . The entire iteration scheme must start with a guess for  $\hat{\sigma}$  or the field  $\mathbf{E}(t)$  and then converges to the dynamics driven by the optimal pulse and the optimal pulse itself.

**B.2. Inclusion of Structural and Energetic Disorder.** If structural and energetic disorder is present, the control field acts simultaneously on molecular systems that differ slightly in regard to their structure and their energy spectrum. Any measured signal appears as a disorder averaging (configuration averaging). This is also valid for the expectation value of the target operator (eq 10), which now reads

$$P_{\text{tar}}(t_f) = \langle \text{tr}_{\text{mx}} \{ \hat{\rho}(t_f) \hat{\Pi}_{\text{tar}} \} \rangle_{\text{config}} = \frac{1}{N_r} \sum_j \sum_{\alpha, \beta} C_{\alpha}^{(j)}(m_{\text{tar}}) C_{\beta}^{(j)*}(m_{\text{tar}}) \rho^{(j)}(\alpha, \beta; t_f) \quad (\text{B6})$$

Disorder averaging is symbolized by  $\langle \dots \rangle_{\text{config}}$  in the first part of the equation and given explicitly in the second part as a summation over all  $N_r$  realizations (the exciton expansion coefficients, as well as the density matrix, must be specified for the concrete disorder configuration). The notation of eq B6 implies that the control kernel (eq B2) takes the form

$$\mathbf{K}(t_f, t; \mathbf{E}) = \frac{i}{\hbar N_r} \sum_j \text{tr}_{\text{mx}} \{ \hat{\sigma}^{(j)}(t) [\hat{\mu}^{(j)}, \hat{\rho}^{(j)}(t)]_- \} \quad (\text{B7})$$

It also includes the disorder averaging. Thus, the optimal pulse is determined as a certain compromise, with respect to all disorder realization. In particular, both density operators ( $\hat{\rho}$  and  $\hat{\sigma}$ ) must be propagated for all disorder realizations simultaneously. This is, of course, numerically very expensive and drastically restricts the number of concrete computations,  $N_r$ .

## References and Notes

- (1) Rice, S. A.; Zhao, M. *Optical Control of Molecular Dynamics*; Wiley: New York, 2000.
- (2) Shapiro, M.; Brumer, P. *Principles of the Quantum Control of Molecular Processes*; Wiley: Hoboken, NJ, 2003.
- (3) Wilson, K. *J. Chem. Phys.* A **1999**, *103*, 10021.
- (4) *Chem. Phys.* **2001**, *267*, 1. (Special issue on laser pulse control.)
- (5) Tannor, D. J.; Kosloff, R.; Rice, S. A. *J. Chem. Phys.* **1986**, *85*, 5805.
- (6) Brumer, P.; Shapiro, M. *Chem. Phys. Lett.* **1986**, *126*, 54.
- (7) Pierce, A. P.; Dahleh, M. A.; Rabitz, H. *Phys. Rev. A* **1988**, *37*, 4950.
- (8) Shi, S.; Woody, A.; Rabitz, H. *J. Chem. Phys.* **1988**, *88*, 6870.
- (9) Zeidler, D.; Frey, S.; Wohlleben, W.; Motzkus, M.; Busch, F.; Chen, T.; Kiefer, W.; Materney, A. *J. Chem. Phys.* **2002**, *116*, 5231.
- (10) Brixner, T.; Damrauer, N. H.; Kiefer, B.; Gerber, G. *J. Chem. Phys.* **2003**, *118*, 3692.
- (11) Herek, J. L.; Wohlleben, W.; Cogdell, R. J.; Zeidler, D.; Motzkus, M. *Nature* **2002**, *417*, 533.
- (12) Mancal, T.; May, V. *Eur. Phys. J. D* **2001**, *14*, 173.
- (13) Mancal, T.; Kleinekathöfer, U.; May, V. *J. Chem. Phys.* **2002**, *117*, 636.
- (14) Ohtsuki, Y.; Zhu, W.; Rabitz, H. *J. Chem. Phys.* **1999**, *110*, 9825.
- (15) van Amerongen, H.; Valkunas, L.; van Grondelle, R. *Photosynthetic Excitons*; World Scientific: Singapore, 2000.
- (16) Rätsep, M.; Blankenship, R. E.; Small, G. J. *J. Phys. Chem. B* **1999**, *103*, 5736.
- (17) Matsuzaki, S.; Zazubovich, V.; Rätsep, M.; Hayes, J. M.; Small, G. J. *J. Phys. Chem. B* **2000**, *194*, 9564.
- (18) Tronrad, D. E.; Matthews, B. W. In *Photosynthetic Reaction Centers*; Deisenhofer, J., Norris, J. R., Eds.; Academic Press: New York, 1993; p 13.

- (19) Renger, Th.; May, V.; Kühn, O. *Phys. Rep.* **2001**, *343*, 137.  
(20) Brüggemann, B.; May, V. *J. Chem. Phys.* **2003**, *118*, 746.  
(21) May, V.; Kühn, O. *Charge and Energy Transfer Dynamics in Molecular Systems*, Second Edition; Wiley–VCH: Weinheim, Germany, 2003.  
(22) Renger, Th.; May, V. *J. Phys. Chem. A* **1998**, *102*, 4381.  
(23) Wendling, M.; Przyjalowski, M. A.; Gülen, D.; Vulto, S. I. E.; Aartsma, T. J.; van Grondelle, R.; van Amerongen, H. *Photo. Res.* **2002**, *71*, 99.  
(24) Brüggemann, B.; May, V. *J. Chem. Phys.* **2004**, *120*, 2325.  
(25) The type of local spectral densities used somewhat contradicts the conclusions of ref 22. However, we showed in this paper that the neglect of a certain delocalization of the FMO protein vibrations does not alter the results (linear absorption, Figure 4 of ref 22) drastically.  
(26) Brüggemann, B.; Herek, J. L.; Sundström, V.; Pullerits, T.; May, V. *J. Phys. Chem. B* **2001**, *105*, 11391.  
(27) Kaiser, A.; May, V. *J. Chem. Phys.*, in press.  
(28) Brüggemann, B.; May, V., manuscript in preparation.  
(29) Ryzhov, I. V.; Kozlov, G. G.; Malyshev, V. A.; Knoester, J. *J. Chem. Phys.* **2001**, *114*, 5322.